Applied Materials Today 41 (2024) 102466

Contents lists available at ScienceDirect

Applied Materials Today

journal homepage: www.elsevier.com/locate/apmt

Tuning the crystallinity of Cu-based electrocatalysts: Synthesis, structure, and activity towards the CO_2 reduction reaction

Nivetha Jeyachandran [a], Wangchao Yuan [a], Xiang Li [a], Akshayini Muthuperiyanayagam [a], Stefania Gardoni [a], Jiye Feng [b], Qingsheng Gao [b], Martin Wilding [e], Peter Wells [d,e], Devis Di Tommaso [a,c], Cristina Giordano [a,*]

[a] Department of Chemistry, Queen Mary University of London, Mile End Road, London E1 4NS, UK
[b] Department of Chemistry, College of Chemistry and Materials Science, Jinan University, Guangzhou 510632, PR China
[c] Digital Environment Research Institute, Queen Mary University of London, Empire House, 67-75 New Road, London E1 1HH, UK
[d] School of Chemistry, University of Southampton, Southampton SO17 1BJ, United Kingdom
[e] Catalysis Hub, Research Complex at Harwell, Rutherford Appleton Laboratory, Chilton OX11 0DE United Kingdom

ARTICLE INFO

Keywords:
Amorphous catalysts
Tuneable crystallinity
Cu nanoparticles
Urea Glass Route
CO_2 reduction reaction

ABSTRACT

The rising levels of CO_2 have spurred growing concerns for our environment, and curbing CO_2 emissions may not be practically viable with the expanding human population. One attractive strategy is the electrochemical CO_2 reduction (CO_2RR) into value added chemicals but because of the chemical inertness of the CO_2 molecule, the electrochemical reduction requires a suitable catalyst. Cu-based catalysts have been largely investigated for CO_2RR, however, the difficulty achieving a high selectivity and faradaic efficiency towards specific products, especially hydrocarbons, is still a challenge, alongside the concern over cost, stability and scarcity of the metal catalyst. The present research focuses on tuning the crystallinity of Cu nanoparticles via a green, cost-friendly, and facile method, called the urea glass route. Remarkably, the incorporation of a selected nitrogen-carbon rich source (namely, 4,5 dicyanoimidazole) at low temperatures allow the formation of an oxidized derived amorphous Cu system, whilst a second thermal treatment enables the transformation to crystalline Cu^0. We found that the combination of surface Cu^0 and Cu^{1+} (observed via XPS studies) present in our amorphous and crystalline Cu nanoparticles leads to interesting differences in the final catalytic activity when tested under CO_2 reaction conditions. The combination of extended X-ray absorption fine structure (EXAFS) experiments and molecular dynamics simulations provides compelling evidence for the amorphous and metallic nature of Cu nanoparticles.

1. Introduction

The electrochemical reduction of CO_2 (CO_2RR) into hydrocarbons and oxygenates such as carbon monoxide (CO), formic acid (HCOOH), methane (CH_4), methanol (CH_3OH) and ethylene (C_2H_4) is an attractive approach to simultaneously alleviate the atmosphere from anthropogenic CO_2 emissions and generate value-added chemicals. The main challenges relate to the high stability of the CO_2 molecule and the competing hydrogen evolution reaction (HER), which lowers the overall selectivity and faradaic efficiency (FE). Both problems can be alleviated using suitable electrocatalysts to activate, and then sustain, the CO_2 reduction, while addressing the reaction toward the least number of products. Another challenge relates to the production of so-called C2+ molecules such as ethylene, ethanol (C_2H_5OH), and *n*-propanol (C_3H_7OH). They are one of the most attractive carbon-based chemicals but face challenges of low current density and poor selectivity due to unsatisfactory catalysts not capable of hydrogenation and C—C coupling reactions [1,2]. The electrochemical conversion of CO_2 proceeds via an multi-electron transfer and proton coupling which leads to variety of gaseous and liquid products [3]. The mechanism for CO_2RR simply involves 3 steps, which are as follows: 1) CO_2 adsorbs onto the catalyst surface, 2) CO_2 is activated and proton transfer occurs, 3) structural rearrangement and desorption takes place. Different metals are classified depending on their binding energy. For instance, metals like Sn, Pb, Hg, and In generate the *OCHO intermediate and thus favour formic acid production. Whilst Cu is unique because it allows the generation of

* Corresponding author.
E-mail address: c.giordano@qmul.ac.uk (C. Giordano).

https://doi.org/10.1016/j.apmt.2024.102466
Received 19 June 2024; Received in revised form 18 September 2024; Accepted 1 October 2024
Available online 9 October 2024

*COH or *CHO intermediates (when the CO_2 molecule binds onto the Cu catalyst), enabling the conversion to such desirable hydrocarbons and alcohols [4].

Metallic Cu has sparked interest towards the CO_2RR [5] due to its ability to convert CO_2 into more than thirty products including C2+ molecules and its relative abundance [6,7]. Nonetheless, crystalline Cu electrocatalysts are not sufficient to attain high FE and selectivity. Numerous investigations have focused on the optimisation of both composition and structure of Cu-based electrocatalyst to improve the overall electrocatalysts performances. These optimizations include surface modification [8,9], metal doping [10,11], alloying [12–14], and nano-structuring [15–17], just to cite some (see also Table 1). Recent research has highlighted the higher selectivity of amorphous Cu nanoparticles (NPs) (namely no medium- to long-range structural order) for formic acid (37 %) and ethanol (22 %) compared to crystalline NPs [18]. This superior performance may originate from the isotropic nature of amorphous materials, where atoms are arranged in a non-periodic lattice assembly, creating disorder within the structure and loose bonds between atoms. The formation of defects and 'dangling' bonds serves as special active sites, allowing the electrochemical reaction to proceed [18]. The benefit of amorphous materials was also observed during the electrochemical reaction, where species initially inactive were converted into active ones, thanks to the structural flexibility of amorphous materials [19]. However, only a few studies have considered amorphous systems in CO_2RR [20], and catalysis in general, due to their structural complexity and difficulties in feature engineering.

There are several strategies to prepare amorphous materials, which, for simplicity, are here divided into physical and chemical methods (Fig. 1). Among physical methods, the "collapse" of the crystal structure can be induced with the aid of high pressure or ball milling [21]. Chemical methods allows to create defects and disorders into the structure *via* chemical reactions, such as doping [22], electrochemical transformation [23], surface modification [24] and more. One of the main benefit of chemical method compared to physical methods is that the synthesis can be more easily controlled with the former than the latter [25].

In the present contribution we introduce a new method to tune the crystallinity of Cu electrocatalysts, starting from a sol-gel based route. The conversion from amorphous to crystalline is simply done by tailoring the composition of precursor, followed by a double thermal treatment. Both amorphous and crystalline systems were characterised experimentally and computationally and tested for CO_2RR to confirm the effect of crystallinity over activity. Preliminary results have shown that crystalline nanoparticles (c-NPs) performed better than the corresponding amorphous nanoparticles (a-NPs).

2. Materials and methods

Copper (II) nitrate trihydrate (puriss. p.a., 99–104 %), Urea (ACS reagent, 99.0–100.5 %), ethanol (Puriss p.a Absolute ≥99.8 %) purchased from Sigma Aldrich. 4,5 Dicyanoimidazole, 99 %, purchased from Thermoscientific.

Table 1
The various amorphous Cu-based catalysts for CO_2RR in the literature.

Composition	FE (%)	Potential (V vs RHE)	Main products	Ref
Amorphous Cu (CuDIR1–350 °C)	8/7	−1.1	CO/C_2H_4	**This work**
Crystalline Cu (CuDIR1–550 °C)	26/16			
Cu R3	15/12			
Amorphous Cu NPs	37 22	−1.4	HCOOH C_2H_6O	[18]
Crystalline Cu NPs	~28		HCOOH	
Amorphous CeO_2-Cu composite	25 7.9	−0.6	CH_3CH_2OH $CH_3CH_2CH_2OH$	[44]

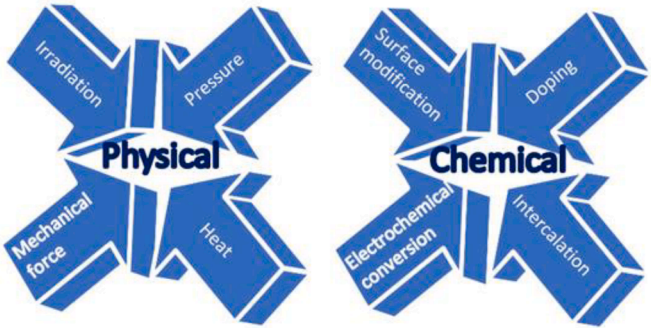

Fig. 1. Different strategies to synthesize amorphous materials.

The standard procedure to prepare Cu^0 nanoparticles is based on a modified sol-gel method known as the Urea Glass Route (UGR), traditionally used for the synthesis of a wide range of products, including metal carbide (MC) and nitrides (MN), and then adapted for the synthesis of bimetallic systems [26], metal oxides (MO), oxynitrides (MON) and just recently pure metal (M^0) nanoparticles [27]. The synthetic pathway to amorphous copper-based system was adjusted from a previously formulated procedure [13]. In this procedure, copper nitrate trihydrate, $Cu(NO_3)_2{\cdot}3H_2O$ is first dissolved in suitable amount of ethanol, resulting in light-blue solutions (Fig. 2). To the resulting solution, a desired amount of urea is added to achieve a specific urea/metal molar ratio (R). This was then heated to 350 °C, under N_2, flow, to obtain crystalline Cu^0, which is later discussed as Cu R3. For comparison, a sample with $R = 0$ (i.e. without the addition of urea) was also prepared. In a second step, 4,5, dicyanoimidazole is added to the alcoholic solution in an amount equivalent to the urea/metal molar ratio. Different strategies were implemented to tune the crystallinity, such as changing temperature, dwelling time, and ramping time (**figure SI.1–2**). In addition, different DI/metal and urea/metal ratios were tested to check its influence on the final phase (**Figure SI.3 and SI.4.**) as this effect was previously observed for other systems [28]. The mixtures were homogenized with the assistance of an ultrasonic bath, leading to blue viscous gel-like precursors. These blue "gels" were then thermally treated under N_2 flow up to 350 °C, resulting (upon cooling) in a black shiny powder. This sample was found to be amorphous as confirmed by XRD (Fig. 3A) and is named CuDIR1_350 °C in the discussion. Then, the as-prepared powders were reheat-treated up to 550 °C, leading to crystalline Cu^0. This sample is further discussed as CuDIR1_550 °C. Characterization of the powders, before and after the second heat-treatment, showed the presence of copper phase but with a complete change in the crystallinity of the final material.

2.1. Electrochemical testing

Electrochemical characterisation

To perform the preliminary qualitative CO_2 tests at first the ink of the catalyst had been prepared mixing the material, 900 μL of DI water, 100 μL of 2-propanol and 50 μL of Nafion and sonicated for one hour. Working electrodes had been prepared by drop-casting 5 μL of ink on glassy carbon (3 mm diameter) electrode and allowed to dry at room temperature for 30 mins in ambient air.

The qualitative CO_2RR tests were performed using a three-electrode cell set-up. The Autolab potentiostat was employed with an Ag/AgCl (3 M KCl) as a reference electrode, and platinum sheet as counter electrode. All the measurements were performed in CO_2 saturated 0.1 M $KHCO_3$ electrolyte at room temperature. Linear sweep voltammetry (LSV) was performed in the range of −2 to -0.6 V (vs. Ag/AgCl) with a scan rate of 500 mV/s. The polarization curves were iR corrected manually.

Products analysis.

All of the current densities were collected by a standard three-

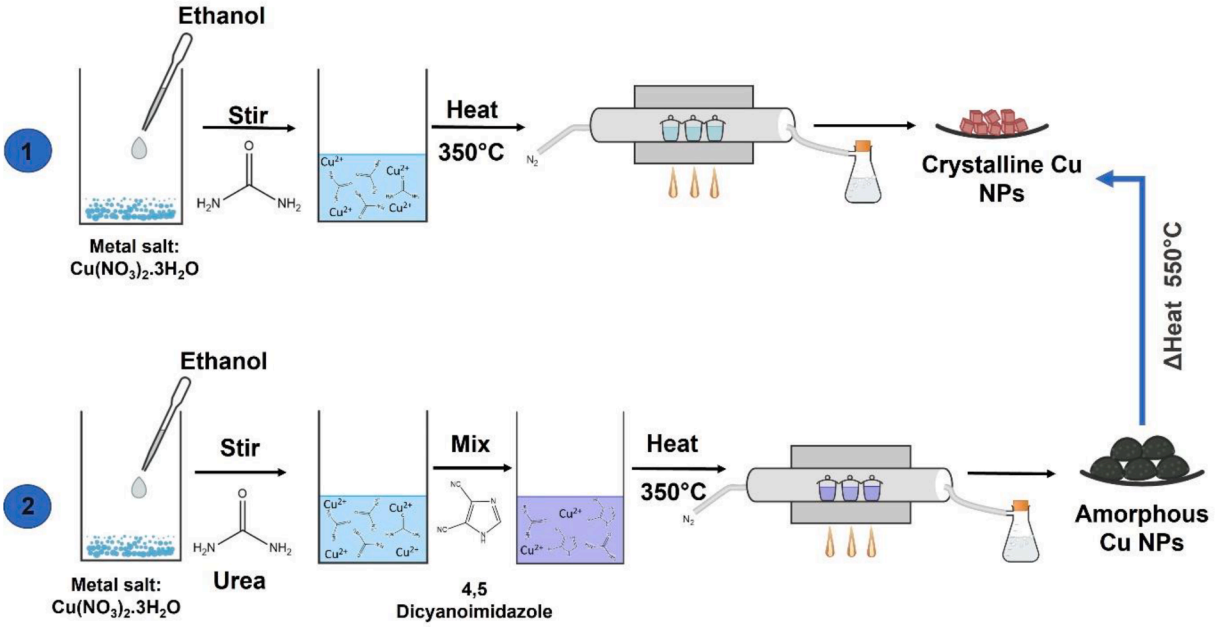

Fig. 2. Schematic preparation steps for the synthesis of amorphous and crystalline Cu system.

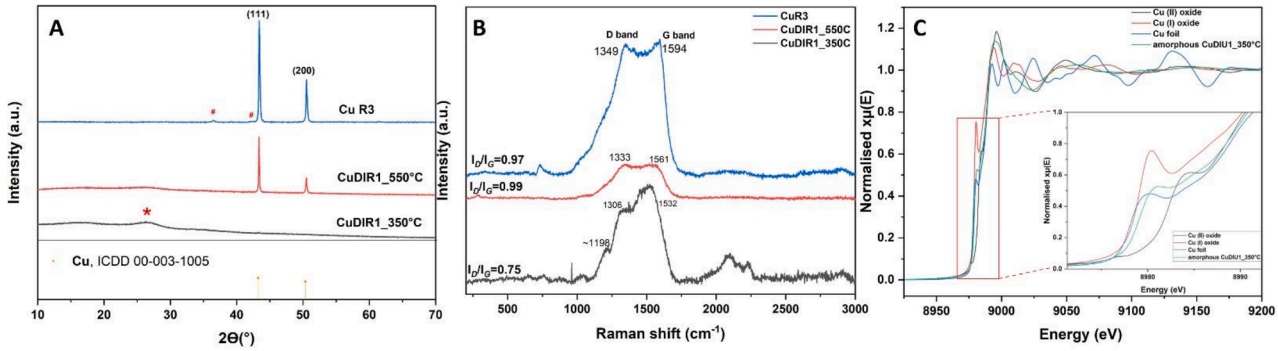

Fig. 3. (A) XRD patterns of CuDIR1 in the presence of urea after first and after second heat-treatment (up to 350 °C and 550 °C, respectively) compared to Cu R3 prepared by classical UGR. Marked (*) peak at 26° is attributed to carbon phase (ICDD 04-015-2407) and Marked peak (#) attributed to Cu_2O (ICDD 01-091-2930). (B) Raman spectra of CuDIR1_350 °C, CuDIR1_550 °C, and Cu R3. (C) Cu K-edge XANES spectra of amorphous CuDIR1_350 °C compared to Cu, Cu_2O and CuO powders diluted in cellulose and enlargement of the Cu K-edge XANES spectra of the absorption edge position (see inset).

electrode configuration on an electrochemical workstation (CHI 660, Shanghai Chenhua), using a Ag/AgCl electrode as the reference electrode, gas diffusion electrode as working electrode and a platinum as the counter electrode. The applied potentials were converted to the RHE using the equation:

$$E(\text{vs.RHE}) = E(\text{vs.Ag/AgCl}) + 0.197\text{V} + 0.0591 \times \text{pH}.$$

For the CO_2RR performance, the catalysts were loaded onto GDL and tested in a flow cell (Gaoss Union). CO_2 with the flow rate of 20 mL min^{-1} was passed through the gas chamber at the back side of the GDL (1×1 cm^2). The quantification of gaseous products was conducted on a gas chromatograph (GC). Gas-phase products were sampled every 20 min using high-purity nitrogen (N_2, 99.999 %) as the carrier gas. The column effluent (separated gas mixtures) was first passed through a thermal conductivity detector (TCD) where hydrogen was quantified; then CO_2RR products was quantified by FID. According to the peak areas in GC, the FEs were calculated using the following equations:

$$FE = \frac{nxFV}{j_{total}} \times 100\%$$

where n is the number of electrons transferred, x is the mole fraction of the product, F is faradaic constant ($F = 96{,}485$ C mol^{-1}), V is the total molar flow rate of gas, and j_{total} is the total current.

Preparation of cathode electrodes. The catalyst ink was prepared by ultrasonically dispersing of 5 mg sample and 50 μL Nafion solution (5%) in 450 μL anhydrous ethanol for 30 min. Then, 100 μL of the as-prepared catalyst ink was drop-coated on the carbon paper electrode ($S = 0.5$ cm $\times$ 2 cm) with a loading of 1 mg/cm^2. The electrode was then dried slowly under room temperature for the subsequent electrochemical tests.

2.2. Computational methods

The molecular dynamics (MD) calculations were conducted using "Vienna ab initio simulation package" (VASP, version 6.4.0) [29]. Interatomic interactions were described using a machine learning force fields (ML-FF) generated *via* the on-the-fly machine learning method implemented in VASP. The ML-FF were learned and trained on-the-fly during an ab-initio MD (AIMD) simulation [30,31] in the constant-pressure, constant-temperature (NPT) ensemble using a Langevin thermostat for temperatures varying from 100 K to 2700 K. The simulations started from a ($3 \times 3 \times 3$) super cell of the copper and

copper oxide bulk structures optimized at the spin-polarized density functional theory (DFT) level of theory with the Perdew–Burke–Ernzerhof (PBE) exchange correlation functional. During the AIMD simulations, a single k-point (1 × 1 × 1) was used together with a plane-wave basis set within the framework of the projector augmented wave method [32]. The kinetic energy cut-off was set to 550 eV. The ML-FF were employed to generate amorphous forms of metallic copper (Cu), copper(I) oxide (cuprous oxide, Cu_2O) and copper(II) oxide (cupric oxide, CuO) using the melt-and-quench method [33]. Starting from the DFT optimized bulk structures, the (3 × 3 × 3) supercells of Cu (108 atoms), Cu_2O (162 atoms) and CuO (216 atoms) were heated to 3000 °C in the NPT ensemble to obtain a liquid phase. Then, we cooled the liquid to an amorphous phase by performing a series of NPT simulations for 40 ps each, decreasing the temperature by 300 K at each step until reaching 300 K. Finally, we equilibrated the amorphous phase for 20 ps at 300 K. The last configuration of the MD trajectory at 300 K was subject to geometry optimisation. The X-ray Absorption Fine Structure (XAFS) spectra of the Cu K-edge was collected at beamline B18 of Diamond Light Source (UK). Monochromatic beam between 6.34 keV and 9.98 keV (kmax = 16) was introduced through a bending magnet and Pt-coated Si(111) double crystal monochromator. The beam size at the sample was approximately 1.0 × 1.0 mm2 and the photon flux was ~1011 pH/s (no attenuation). The XAFS spectra were collected in transmission mode, and the intensity of the incident beam (I0) and the transmitted beam (It) was monitored by ionization chambers (filled with a mixture of He, N_2, and Ar). Samples were diluted with cellulose before pressing into 13 mm diameter pellet and the XAFS spectra of each sample were measured for at least 3 times and merged to improve the signal-to-noise ratio. Metal foil was measured simultaneously for each sample as a reference for energy calibration. XAFS data was analyzed using the Demeter software package (including Athena and Artemis, version 0.9.26).

3. Results and discussion

3.1. Bulk structure and ordering

The phase composition of the as-prepared powders was investigated via X-rays diffraction (XRD, wide angle). Fig. 3 reports the XRD, Raman and EXAFS of the materials prepared with the assistance of DI after the first and second heat treatment.

The XRD patterns of the CuDIR1 samples (prepared with urea) (Fig. 3a) show that the addition of 4,5 dicyanoimidazole leads to no crystalline phases (no diffraction peaks are observed) and only an amorphous phase, attributed to a carbon content (broad peak around 26°, ICDD 04-015-2407) is seen. On the other hand, it can be observed that the samples prepared using urea in the absence of 4,5 dicyanoimidazole only are made by a crystalline Cu phase (ICDD 00-003-1005), regardless of the urea/metal ratio (R). However, it can be also noted that with increasing the urea/metal molar ratio, a slight reduction in the intensity of the peaks occurs, somehow indicating a decrease in crystallinity (**see SI.4**). The effect of increasing urea/metal ratio is more visible on peak broadness, which increases going from $R = 0$, 3, and 5 (FWHM = 0.13400, 0.19138 and 0.23252, respectively), indicating again a lower degree of crystallinity or smaller sized nanoparticles (**see Table SI.6**). We observe a small peak on Cu R3 marked as (#) which is identified as Cu_2O (ICDD 01-091-2930), possibly due to surface passivation. Increasing both the DI amount and R led to the sharpening of the carbon peak, which became more prominent with increasing DI/R ratios, but no peaks attributable to any Cu species can be observed **(Figure SI.3.)**. Yet, the presence of Cu in the amorphous samples was confirmed by SEM-EDX investigation (**Figure SI.5–6**). Interestingly, when the amorphous CuDIR1 (presence of urea) undergoes a second heat-treatment, a crystalline Cu phase is formed. The second heat-treatment influenced the carbon phase too, with a noticeable decrease of the peak intensity (*marked peak, ~26°). Clearly, the second heat-treatment serves to remove the excess carbon phase. EDS investigation seems to confirm this observation, and a C reduction (from 29 wt% to 17.3 wt%) was observed for the amorphous CuDI1R1 samples, before and after second heat treatment, respectively (**Figure SI.6–8)**. This outcome supports the conclusion that the partial release of the carbon matrix is contributing to the crystallisation of Cu. Here it is important to mention that the one-step heat treatment only, directly up to 550 °C, resulted in the formation of crystalline Cu^0 (**figure SI.9**).

Raman spectroscopy is a useful tool to deduce the structure, particularly defects and the disorder nature of the Cu-based samples. The Raman spectra of the samples exhibit two distinct peaks at around 1306 cm^{-1}–1349 cm^{-1} and 1532–1594 cm^{-1} corresponding to well defined D band and G band (Fig. 3b), respectively. The intensity ratio of the D and G bands (I_D/I_G ratio) allows to estimate the defects of Cu based samples where a higher ratio ensures more defects on Cu [34]. The calculated I_D/I_G ratios of CuDIR1_350 °C, CuDIR1_550 °C and Cu R3 are 0.75, 0.99, and 0.97 respectively. Interestingly, a higher I_D/I_G ratio is seen for the crystalline Cu samples (i.e. Cu R3 and CuDIR1_550 °C) compared to amorphous Cu (CuDIR1_350 °C) which depicts the defective nature on the carbon for both crystalline samples compared to amorphous Cu system. Interestingly, we also observe a shoulder about ~1198 cm^{-1} on the CuDIR1_350 °C (amorphous Cu) which is attributed to the disorder sp3 carbon phase. [35] The shoulder observed for CuDIR1_350 °C (amorphous Cu) appears to be more prominent compared to the crystalline Cu samples. In order to understand the coordination environment of Cu in the amorphous and reheated crystalline Cu system, X-ray absorption near edge structure (XANES) and extended X-ray absorption fine structure (EXAFS) were performed. As shown in Fig. 3**C (see inset)**, the absorption edge position of amorphous CuDIR1 is located between the standard references of Cu foil and CuO, indicating the valence state of Cu atoms in the amorphous Cu system is higher than metallic Cu^0 possibly suggesting an oxidized derived Cu system. However, the XAS measurement of the reheated crystalline Cu seems to confirm the presence of metallic Cu^0 (**Figure SI.10).** The XAS data shows that the amorphous CuDIR1_350 °C is closer to CuO standard, while the reheated CuDIR1_550 °C sample is closer to the foil pattern (Cu) (**Figure SI.11**).

The total radial distribution function (RDF) of Cu, Cu_2O, and CuO in Fig. 4 generated by the melt-and-quench MD simulations shows the absence of medium- and long-range order typical of a crystalline phase, confirming their amorphous structure. The first peak at 1.88 Å for amorphous Cu_2O and 1.94 Å for amorphous CuO corresponds to the average Cu-O bond length of the first shell. The peak at 2.49 Å for amorphous metallic Cu corresponds to the average Cu-Cu bond length. The subsequent RDF peaks of both amorphous copper oxides and metallic copper are broadened, due to the loss of long-range crystal ordering in their amorphous structures. The comparison between experimental EXAFS (Fig. 4**(a, up)**) and computational (Fig. 4**(b, down)**) data seems to confirm the presence of different oxidation state for copper in the Cu-based amorphous structure. The first peak at 1.45 Å in the experimental RDF is attributed to the Cu-C bond based on the results by Shi et al. [36], who observed a major peak at 1.48 Å. The peak around 2.4 Å is likely to be that of the Cu-Cu bond, as it matches the MD predicted RDF of amorphous Cu, where the first peak is at 2.5 Å. Moreover, amorphous Cu has a minimum at 3.5 Å based on the computational RDF, which is also reflected in the experimental RDF, where there is also a minimum around 2.9 Å, further confirming the presence of amorphous Cu. The EXAFS spectrum might confirm the presence of Cu_2O. The first peak for Cu_2O in the computational RDF is around 1.88 Å. However, in the experimental RDF, this peak may be merged with the Cu-C peak at 1.45 Å and the Cu-Cu peak at 2.49 Å. Nevertheless, the comparative analysis of the experimental and computational RDFs confirms the presence of a Cu-based amorphous system, consisting of a mixture of Cu-C, Cu-Cu, and Cu-O bonds.

Electrocatalytic CO_2 reduction reaction

The electrochemical performance was tested on the samples and the LSV and faradaic efficiencies are shown in Fig. 5a and b. The LSV shows

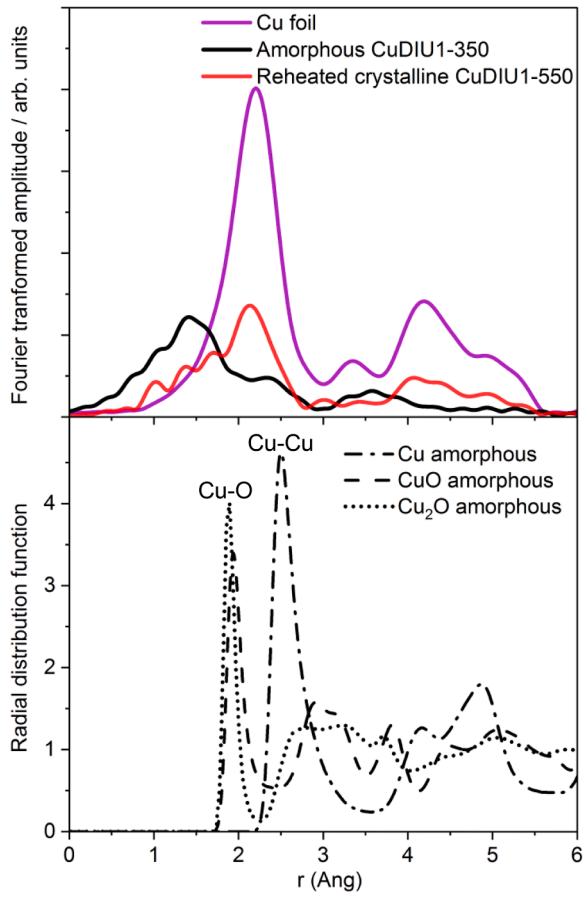

Fig. 4. (a, up) The Fourier transform curves in the *r* space of amorphous CuDIR1 and reheated crystalline CuDIR1 compared to the Cu foil. (b, down) Radial distribution function of the amorphous forms of metallic copper (Cu), copper(I) oxide (Cu_2O) and copper(II) oxide (CuO) obtained from melt-and-quench MD simulations.

that current density reaches around −30 mA/cm^2 for Cu R3 (Black curve), −20 mA/cm^2 for CuDIR1_350 °C (Amorphous, Red Curve) and around −35 mA/cm^2 for CuDIR1_550 °C (reheated, green curve). The reheated crystalline CuDIUR1_550 °C has the highest current density (more negative, about −35 mA/cm^2 at −1.5 V) indicating the highest CO_2RR activity in terms of electron transfer and shows the best performance in CO_2RR, as it produces more valuable CO (26%) and C_2H_4 (16%) compared to other samples. It must be pointed out, however, that the amorphous CuDIR1 might have been affected by the drop casting preparation methods, which lead to some inhomogeneity on the surface of the working electrode and allowed a lower loading of materials on the glassy carbon tip. We observe both crystalline Cu R3 (classical UGR) and reheated CuDIR1 (modified UGR) present a better selectivity towards CO compared to the amorphous CuDIR1 (Fig. 5b). Surprisingly, there is a significant increase in hydrogen for the amorphous CuDIR1 compared to the reheated crystalline CuDIR1.

Activity could be further increased by introducing more active sites, as previously demonstrated [13]. In fact, it was expected to observe an improved performance from the amorphous Cu compared to crystalline Cu, considering that the intrinsic irregular atomic structures of amorphous CuDIR1 should hold more defect sites, larger active surface, faster mass transfer and a stronger CO_2 adsorption [18,37]. However, more sophisticated techniques are needed to rationalize this result, alongside the effect of the competitive HER.

Surface composition and morphology

To have a better understanding of the surface composition in the amorphous samples, X-ray photoelectron microscopy (XPS) was performed. The full scan survey XPS analysis in **Tables SI.1 and SI.2** indicated the presence of Cu, C, N and O elements in the amorphous samples. Fig. 6a (top) shows the high-resolution Cu 2p XPS spectra of the amorphous CuDI1R1. For the as-prepared amorphous Cu nano-catalyst, we observe Cu^0/Cu^{1+} at 932.82 eV and 952.5 eV along with Cu^{2+} located at 935.31 eV and 954.98 eV. In fact, distinguishing Cu^{1+} from Cu^0 via XPS is not trivial due to similar binding energies [38]. The Cu^{2+} is possibly derived from $Cu(OH)_2$, usually expected at 935 eV [39]. Interesting to note, by comparing the high-resolution Cu 2p spectra of both amorphous and crystalline Cu (Fig. 6b, bottom), a visible chemical shift is observed to lower binding energy after the second heat treatment to 932.58 eV and 952.37 eV attributed to Cu^0 along with Cu^{2+} located at 934.84 eV and 954.26 eV [40]. In addition, a lower amount of Cu^{2+} species is observed in the reheated (crystalline) Cu, which could be attributed to CuO arising from a possible surface passivation [41]. Interestingly, we also observe higher content of Cu^0/Cu^{1+}, at least on the surface, in both reheated Cu (in presence of DI) and crystalline Cu (without DI, see **Figure SI.12**), compared to the amorphous Cu. This could explain the better catalytic activity observed in the crystalline Cu system, compared to amorphous Cu, since the presence of more Cu^0 and Cu^{1+} is found to have a positive influence on the catalytic activity, as observed by Xiao et al. [42], who also demonstrated how the synergy between the surfaces of both Cu^{1+} and Cu^0 results in greater kinetics and thermodynamics for both CO_2 activation and CO dimerization, ultimately enhancing activity toward the CO_2RR. Another interesting result

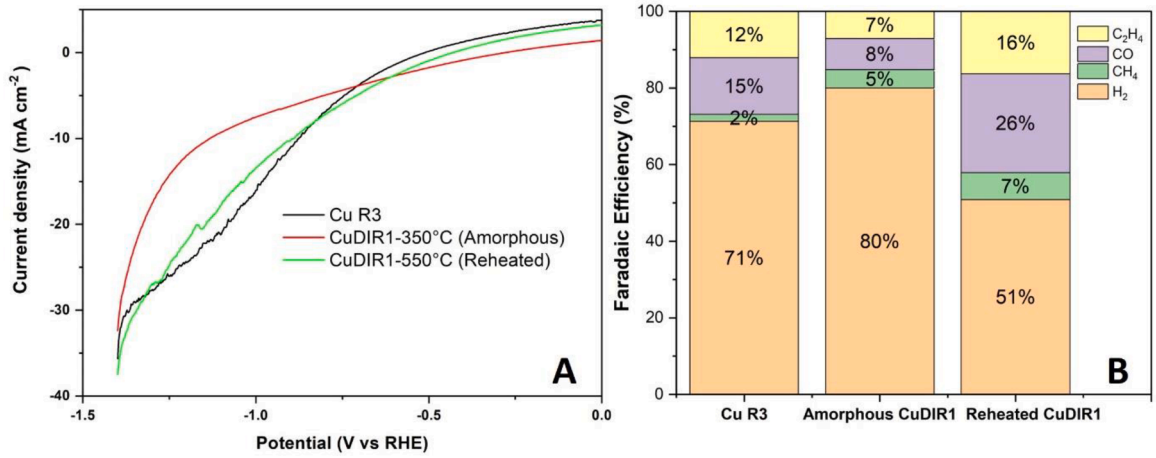

Fig. 5. Performance in electrocatalytic CO_2RR on Cu R3, CuDIR1–350 °C (amorphous) and CuDIR1–550 °C (reheated) of LSV (A) and Faradaic efficiencies of different products at the potential of −1.1 V vs RHE (B).

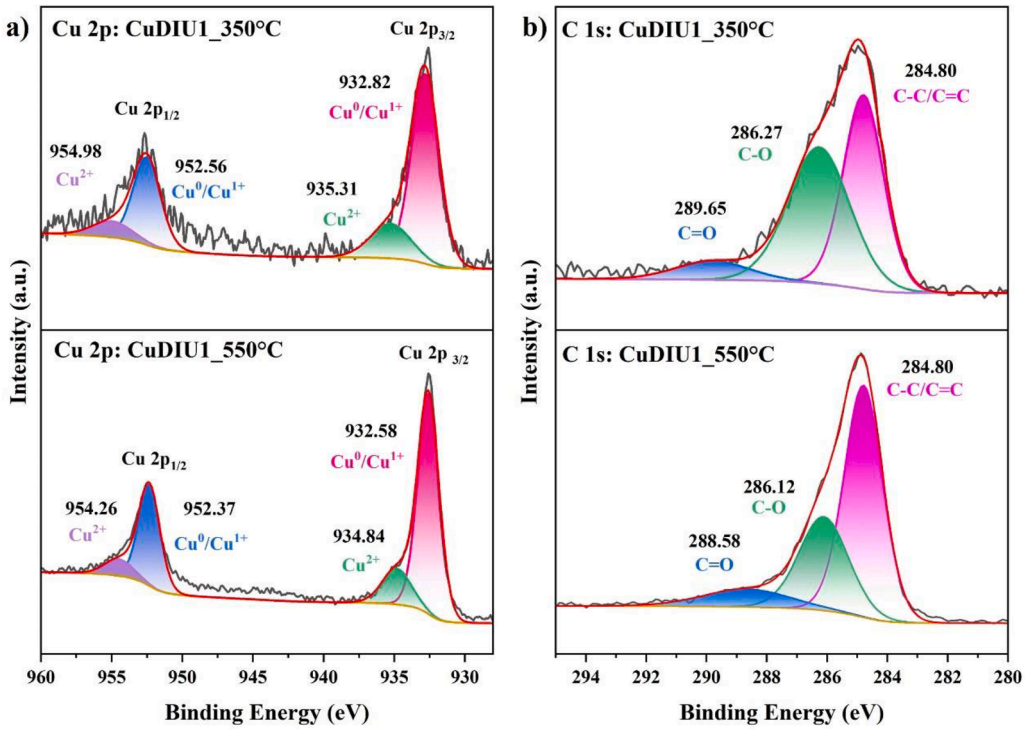

Fig. 6. XPS showing high resolution of (a) Cu 2p spectra of amorphous CuDI1R1–350 °C (top) and after second heat treatment of reheated crystalline CuDIR1_550 °C (bottom). (b) C 1 s spectra of amorphous CuDI1R1–350 °C (top) and after second heat treatment of reheated crystalline CuDI1R1–550 °C (bottom).

of the combination of surface Cu^0 and Cu^{1+} (during the CO_2RR) is that the pathway to C2+ is more favoured than the one to C1 products, allowing the possibility to obtain more complex molecules, which are one of the current challenges till this day. Further investigation was performed on the high-resolution C 1 s spectra (Fig. 6B). It was observed that for the as-prepared amorphous Cu, the peak located at ~286 eV had a higher content of C—O compared to after the second heat treatment (**Table SI.5**). The peak at 284.80 eV can be ascribed C—C/C = C (28.88 at%), however, after the second heat treatment, we observed a larger area (34.62 at%) at 284.80 eV, which was attributed to the sp^2 hybridised C = C (graphitised carbon) [43]. In addition, XPS confirmed that the amount of carbon, at least on the surface, is greater for samples prepared in the presence of both DI and urea than in the presence of DI only (i.e. in the absence of urea), as expected and shown in **Tables SI.1.-SI.4**.

SEM investigation revealed some differences between the as-prepared amorphous and crystalline samples and marked morphological changes can be observed (**Figure SI.13**). After the second heat treatment, the formation of particles on the surface can be observed; these particles were identified as Cu by EDX mapping (**Figure SI.7–8**). Remarkably, when the amorphous samples were prepared at a higher DI/R (e.g. molar ratio = 5), a visible difference on morphology was seen, with the formation of spheroidal particles on the surface (**figure SI.14**), rather than the porous-like structure observed for lower DI/R molar ratio (e.g. molar ratio 1). Clearly, the concurrent increasing of the urea/metal and DI/metal molar ratio has an influence on the material final morphology. Further characterizations were also performed, including FT-IR and TGA, to confirm the different nature of the starting gels

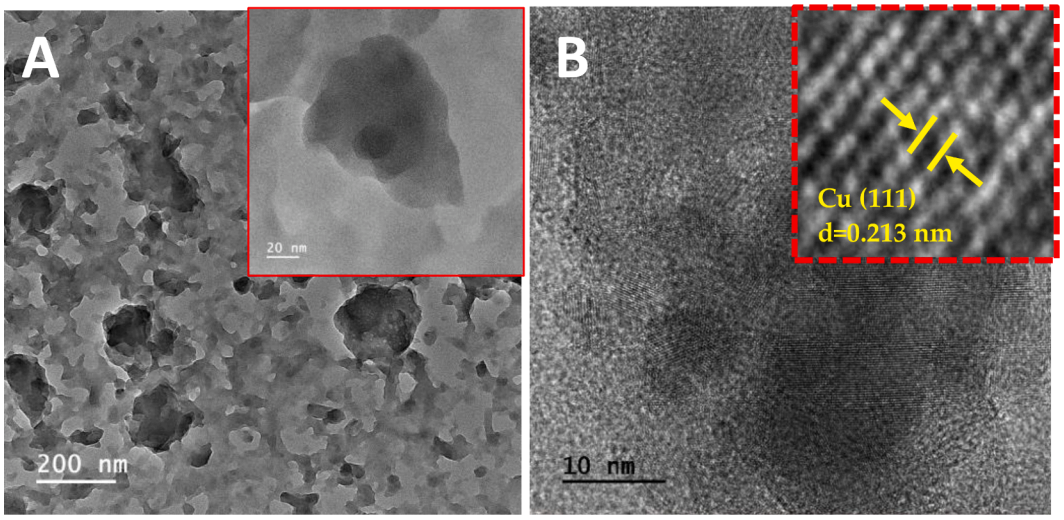

Fig. 7. HR-TEM images of CuDIR1 after the first (A) and the second (B) heat-treatment, respectively

prepared with and without urea and/or DI assistance (**Figure SI.15–16**).

The different appearance of the samples prepared with DI (in presence of urea) before and after the second heat-treatment can be observed by TEM investigation (Fig. 7). While the double treated sample shows the presence of lattice fringes confirming the presence of crystallinity, the sample after one treatment only, showed a "cloud-like" structure, no lattice fringes and particles are observed (Fig. 7a), somehow indicating its amorphous nature.

4. Conclusions

In this study, a facile, cost-effective, and eco-friendly pathway to synthesize amorphous oxidized-derived Cu catalyst at low temperatures ($T = 350$ °C) is presented. We have showed how the incorporation of the nitrogen-carbon rich 4,5 dicyanoimidazole (DI) can help to tune the crystallinity and morphology of the final nanoparticles, going from amorphous to highly crystalline Cu^0 nanoparticles. The structural (amorphous *vs* crystalline) and compositional (metallic *vs* oxide) properties of the Cu nanoparticles were revealed by a combination of EXAFS and MD simulations, which confirmed the medium- and long-range disorder and the presence of both oxides and metallic Cu in the samples.

In our study, we also investigated the role of crystallinity in the CO_2 reduction reaction (CO_2RR) by exploring the performance of amorphous to crystalline Cu catalysts synthesized using our novel Urea Glass Route procedure. The Cu-based catalysts were tested for CO_2RR but, contrary to expectation, the crystalline system showed better catalytic activity towards CO_2RR, based on LSV electrochemical characterisation. To explain this behaviour XPS studies were performed, showing a higher content of surface Cu^0/Cu^{1+} in the crystalline Cu system compared to the amorphous Cu-based catalyst, somehow indicating a positive effect with regards to the catalytic activity. We can then hypothesise that the presence in the material surface of both surface Cu^0 and Cu^{1+} creates a synergistic effect enabling CO_2 activation and CO dimerization to occur faster, hence boosting the CO_2RR. Interestingly, the CO_2RR performance of reheated crystalline Cu NPs, prepared with the assistance of DI and a double-step heat treatment, showed a better selectivity toward CO compared to amorphous Cu system and crystalline Cu R3 (prepared via traditional urea without DI). As observed, the transition from amorphous oxidized Cu catalyst (prepared at 350 °C) to crystalline Cu^0 phase (prepared at 550 °C), the degree of crystallinity appears to influence product distribution. We acknowledge that the current catalytic performance of our Cu-based catalysts, specifically the faradaic efficiency for C2+ products, is lower compared to other reported Cu based catalysts. Our findings demonstrate that the transition from amorphous to crystalline phases in Cu catalysts introduces significant structural and catalytic changes, which provide important insights into how crystallinity influences product selectivity and catalytic behavior in CO_2RR. Our data suggests that different heat treatments leading to different crystal phases could play a role in the catalyst's selectivity. The results presented in this study suggest that the structural properties of the Cu NPs play a major role in tuning the catalytic activity, more than surface area itself.

Funding

NJ acknowledges mini-Centre-for-Doctoral-Training in CO_2—Conversion@QMUL for PhD scholarship. WY&XL acknowledges the Chinese-Council-Scholarship for PhD scholarship. DDT and AM are grateful to the UK Materials and Molecular Modelling Hub for computational resources, which is partially funded by EPSRC (EP/P020194/1). This research utilized Queen Mary's Apocrita HPC facility, supported by QMUL Research-IT. http://doi.org/10.5281/zenodo.438045. SG acknowledges Erasmus programme for the scholarship.

CRediT authorship contribution statement

Nivetha Jeyachandran: Writing – review & editing, Writing – original draft, Validation, Investigation, Data curation. **Wangchao Yuan:** Writing – review & editing, Writing – original draft, Validation, Investigation, Data curation. **Xiang Li:** Writing – review & editing, Writing – original draft, Validation, Investigation, Data curation. **Akshayini Muthuperiyanayagam:** Writing – review & editing, Validation, Methodology, Investigation, Data curation. **Stefania Gardoni:** Writing – review & editing, Data curation. **Jiye Feng:** Writing – review & editing, Data curation. **Qingsheng Gao:** Writing – review & editing, Supervision, Resources, Data curation. **Martin Wilding:** Writing – review & editing, Resources, Data curation. **Peter Wells:** Writing – review & editing, Resources, Data curation. **Devis Di Tommaso:** Writing – review & editing, Writing – original draft, Validation, Supervision, Resources, Project administration, Methodology, Funding acquisition, Data curation, Conceptualization. **Cristina Giordano:** Writing – review & editing, Writing – original draft, Validation, Supervision, Resources, Project administration, Methodology, Funding acquisition, Data curation, Conceptualization.

Declaration of competing interest

The authors declare that they have no known competing financial interests or personal relationships that could have appeared to influence the work reported in this paper.

Data availability

Data will be made available on request.

Acknowledgments

XRD and XPS measurements were performed thanks to the Material Research Institute of QMUL. SEM and TEM experimental data were acquired at the Nanovision facility at QMUL. XAFS data was collected at the B18 beamline at Diamond Light Source as part of the UK Catalysis Hub block allocation for beamtime (SP29721-6).

Supplementary materials

Supplementary material associated with this article can be found, in the online version, at doi:10.1016/j.apmt.2024.102466.

References

[1] R. Yang, Z. Zeng, Z. Peng, J. Xie, Y. Huang, Y. Wang, Amorphous urchin-like copper@nanosilica hybrid for efficient CO2 electroreduction to C2+ products, J. Energy Chem. 61 (2021) 290–296, https://doi.org/10.1016/j.jechem.2020.12.032.

[2] J. Wang, H.-Y. Tan, Y. Zhu, H. Chu, H.M. Chen, Linking the dynamic chemical state of catalysts with the product profile of electrocatalytic CO2 reduction, Angewandte Chemie 133 (2021) 17394–17407, https://doi.org/10.1002/ange.202017181.

[3] N. Jeyachandran, W. Yuan, C. Giordano, Cutting-Edge Electrocatalysts for CO2RR, Molecules. 28 (2023) 3504, https://doi.org/10.3390/molecules28083504.

[4] D. Bhalothia, D.-W. Lee, G.-P. Jhao, H.-Y. Liu, Y. Jia, S. Dai, K.-W. Wang, T.-Y. Chen, Reaction pathways for the highly selective and durable electrochemical CO2 to CO conversion on ZnO supported Ag nanoparticles in KCl electrolyte, Appl. Surf. Sci. 608 (2023) 155224, https://doi.org/10.1016/j.apsusc.2022.155224.

[5] L. Zaza, K. Rossi, R. Buonsanti, Well-defined copper-based nanocatalysts for selective electrochemical reduction of CO $_2$ to C $_2$ products, ACS. Energy Lett. 7 (2022) 1284–1291, https://doi.org/10.1021/acsenergylett.2c00035.

[6] Q. Li, W. Zhu, J. Fu, H. Zhang, G. Wu, S. Sun, Controlled assembly of Cu nanoparticles on pyridinic-N rich graphene for electrochemical reduction of CO2 to ethylene, Nano Energy 24 (2016) 1–9, https://doi.org/10.1016/j.nanoen.2016.03.024.

[7] Copper Demand and Long-Term Availability - Copper Alliance, https://copperalliance.org/(n.d.). https://copperalliance.org/sustainable-copper/about-copper/cu-demand-long-term-availability/ (accessed March 5, 2023).

[8] S. Shen, J. He, X. Peng, W. Xi, L. Zhang, D. Xi, L. Wang, X. Liu, J. Luo, Stepped surface-rich copper fiber felt as an efficient electrocatalyst for the CO2RR to

formate, J. Mater. Chem. A 6 (2018) 18960–18966, https://doi.org/10.1039/c8ta04758h.
[9] Z.-Y. Zhang, H. Tian, H. Jiao, X. Wang, L. Bian, Y. Liu, N. Khaorapapong, Y. Yamauchi, Z.-L. Wang, SiO 2 assisted Cu 0 –Cu + –NH 2 composite interfaces for efficient CO 2 electroreduction to C 2+ products, J. Mater. Chem. A 12 (2024) 1218–1232, https://doi.org/10.1039/D3TA05652J.
[10] Y. Yang, M.G. White, P. Liu, Theoretical study of methanol synthesis from CO 2 hydrogenation on metal-doped Cu(111) surfaces, J. Phys. Chem. C 116 (2012) 248–256, https://doi.org/10.1021/jp208448c.
[11] J. Dean, Y. Yang, N. Austin, G. Veser, G. Mpourmpakis, Design of copper-based bimetallic nanoparticles for carbon dioxide adsorption and activation, ChemSusChem. 11 (2018) 1169–1178, https://doi.org/10.1002/cssc.201702342.
[12] W. Xiong, J. Yang, L. Shuai, Y. Hou, M. Qiu, X. Li, M.K.H. Leung, CuSn alloy nanoparticles on nitrogen-doped graphene for electrocatalytic CO $_2$ reduction, ChemElectroChem. 6 (2019) 5951–5957, https://doi.org/10.1002/celc.201901381.
[13] W. Yuan, N. Jeyachandran, T. Rao, A. Ghulam Nabi, M. Bisetto, D. Di Tommaso, T. Montini, C. Giordano, study on the structure vs activity of designed non-precious metal electrocatalysts for CO2 conversion, Mater. Lett. 341 (2023) 134167, https://doi.org/10.1016/j.matlet.2023.134167.
[14] D. Bhalothia, W.-H. Hsiung, S.-S. Yang, C. Yan, P.-C. Chen, T.-H. Lin, S.-C. Wu, P.-C. Chen, K.-W. Wang, M.-W. Lin, T.-Y. Chen, Submillisecond laser annealing induced surface and subsurface restructuring of Cu–Ni–Pd trimetallic nanocatalyst promotes thermal CO2 reduction, ACS Appl. Energy Mater. 4 (2021) 14043–14058, https://doi.org/10.1021/acsaem.1c02823.
[15] R. Reske, H. Mistry, F. Behafarid, B. Roldan Cuenya, P. Strasser, Particle size effects in the catalytic electroreduction of CO2 on Cu nanoparticles, J. Am. Chem. Soc. 136 (2014) 6978–6986, https://doi.org/10.1021/ja500328k.
[16] B. Yang, C. Liu, A. Halder, E.C. Tyo, A.B.F. Martinson, S. Seifert, P. Zapol, L. A. Curtiss, S. Vajda, Copper cluster size effect in methanol synthesis from CO2, J. Phys. Chem. C 121 (2017) 10406–10412, https://doi.org/10.1021/acs.jpcc.7b01835.
[17] L. Bian, Z.-Y. Zhang, H. Tian, N.-N. Tian, Z. Ma, Z.-L. Wang, Grain boundary-abundant copper nanoribbons on balanced gas-liquid diffusion electrodes for efficient CO2 electroreduction to C2H4, Chinese J. Catal. 54 (2023) 199–211, https://doi.org/10.1016/S1872-2067(23)64540-1.
[18] Y.-X. Duan, F.-L. Meng, K.-H. Liu, S.-S. Yi, S.-J. Li, J.-M. Yan, Q. Jiang, Amorphizing of Cu nanoparticles toward highly efficient and robust electrocatalyst for CO2 reduction to liquid fuels with high faradaic efficiencies, Adv. Mater. 30 (2018) 1706194, https://doi.org/10.1002/adma.201706194.
[19] Y. Jin, M. Zhang, L. Song, M. Zhang, Research advances in amorphous-crystalline heterostructures toward efficient electrochemical applications, Small. n/a (n.d.) 2206081. https://doi.org/10.1002/smll.202206081.
[20] Y. Zhou, H.J. Fan, Progress and challenge of amorphous catalysts for electrochemical water splitting, ACS Mater. Lett. 3 (2021) 136–147, https://doi.org/10.1021/acsmaterialslett.0c00502.
[21] A. Qiao, H. Tao, Y. Yue, Enhancing ionic conductivity in Ag3PS4 via mechanical amorphization, J. Non. Cryst. Solids. 521 (2019) 119476, https://doi.org/10.1016/j.jnoncrysol.2019.119476.
[22] H. Yang, Z. Chen, P. Guo, B. Fei, R. Wu, B-doping-induced amorphization of LDH for large-current-density hydrogen evolution reaction, Appl. Catal. B: Environ. 261 (2020) 118240, https://doi.org/10.1016/j.apcatb.2019.118240.
[23] D. González-Flores, I. Sánchez, I. Zaharieva, K. Klingan, J. Heidkamp, P. Chernev, P.W. Menezes, M. Driess, H. Dau, M.L. Montero, Heterogeneous water oxidation: surface activity versus amorphization activation in cobalt phosphate catalysts, Angewandte Chemie Int. Ed. 54 (2015) 2472–2476, https://doi.org/10.1002/anie.201409333.
[24] H. Cheng, N. Yang, G. Liu, Y. Ge, J. Huang, Q. Yun, Y. Du, C.-J. Sun, B. Chen, J. Liu, H. Zhang, Ligand-exchange-induced amorphization of pd nanomaterials for highly efficient electrocatalytic hydrogen evolution reaction, Adv. Mater. 32 (2020) 1902964, https://doi.org/10.1002/adma.201902964.
[25] K. Hachem, M.J. Ansari, R.O. Saleh, H.H. Kzar, M.E. Al-Gazally, U.S. Altimari, S. A. Hussein, H.T. Mohammed, A.T. Hammid, E. Kianfar, Methods of chemical synthesis in the synthesis of nanomaterial and nanoparticles by the chemical deposition method: a review, BioNanoSci 12 (2022) 1032–1057, https://doi.org/10.1007/s12668-022-00996-w.
[26] X. Li, C. Giordano, Designed NiMoC@C and NiFeMo2C@C core-shell nanoparticles for oxygen evolution in alkaline media, Front. Chem. 11 (2023), https://doi.org/10.3389/fchem.2023.1162675.
[27] C. Giordano, C. Erpen, W. Yao, B. Milke, M. Antonietti, Metal nitride and metal carbide nanoparticles by a soft urea pathway, Chem. Mater. 21 (2009) 5136–5144, https://doi.org/10.1021/cm9018953.
[28] C. Giordano, A. Kraupner, I. Fleischer, C. Henrich, G. Klingelhöfer, M. Antonietti, Non-conventional Fe3C-based nanostructures, J. Mater. Chem. 21 (2011) 16963–16967, https://doi.org/10.1039/C1JM11744K.
[29] G. Kresse, J. Furthmüller, Efficiency of ab-initio total energy calculations for metals and semiconductors using a plane-wave basis set, Comput. Mater. Sci. 6 (1996) 15–50, https://doi.org/10.1016/0927-0256(96)00008-0.
[30] R. Jinnouchi, F. Karsai, G. Kresse, On-the-fly machine learning force field generation: application to melting points, Phys. Rev. B 100 (2019) 014105, https://doi.org/10.1103/PhysRevB.100.014105.
[31] X. Li, W. Paier, J. Paier, Machine learning in computational surface science and catalysis: case studies on water and metal–oxide interfaces, Front. Chem. 8 (2020). https://www.frontiersin.org/articles/10.3389/fchem.2020.601029 (accessed March 28, 2023).
[32] G. Kresse, D. Joubert, From ultrasoft pseudopotentials to the projector augmented-wave method, Phys. Rev. B 59 (1999) 1758–1775, https://doi.org/10.1103/PhysRevB.59.1758.
[33] K.V. Tian, G.A. Chass, D.D. Tommaso, Simulations reveal the role of composition into the atomic-level flexibility of bioactive glass cements, Phys. Chem. Chem. Phys. 18 (2015) 837–845, https://doi.org/10.1039/C5CP05650K.
[34] T. Palaniselvam, H.B. Aiyappa, S. Kurungot, An efficient oxygen reduction electrocatalyst from graphene by simultaneously generating pores and nitrogen doped active sites, J. Mater. Chem. 22 (2012) 23799–23805, https://doi.org/10.1039/C2JM35128E.
[35] D. Varshney, J. Palomino, J. Gil, O. Resto, B.R. Weiner, G. Morell, New route to the fabrication of nanocrystalline diamond films, J. Appl. Phys. 115 (2014) 054304, https://doi.org/10.1063/1.4863822.
[36] G. Shi, Y. Xie, L. Du, X. Fu, X. Chen, W. Xie, T.-B. Lu, M. Yuan, M. Wang, Constructing Cu−C bonds in a graphdiyne-regulated cu single-atom electrocatalyst for CO2 reduction to CH4, Angewandte Chemie Int. Ed. 61 (2022) e202203569, https://doi.org/10.1002/anie.202203569.
[37] F. Hu, L. Yang, Y. Jiang, C. Duan, X. Wang, L. Zeng, X. Lv, D. Duan, Q. Liu, T. Kong, J. Jiang, R. Long, Y. Xiong, Ultrastable Cu catalyst for CO2 electroreduction to multicarbon liquid fuels by tuning C–C coupling with CuTi subsurface, Angewandte Chemie Int. Ed. 60 (2021) 26122–26127, https://doi.org/10.1002/anie.202110303.
[38] T. Ghodselahi, M.A. Vesaghi, A. Shafiekhani, A. Baghizadeh, M. Lameii, XPS study of the Cu@Cu2O core-shell nanoparticles, Appl. Surf. Sci. 255 (2008) 2730–2734, https://doi.org/10.1016/j.apsusc.2008.08.110.
[39] X. Wang, B. Zhang, W. Zhang, M. Yu, L. Cui, X. Cao, J. Liu, Super-light Cu@Ni nanowires/graphene oxide composites for significantly enhanced microwave absorption performance, Sci. Rep. 7 (2017) 1584, https://doi.org/10.1038/s41598-017-01529-2.
[40] J.F. Moulder, Handbook of X-ray photoelectron spectroscopy: a reference book of standard spectra for identification and interpretation of XPS data, physical electronics division, Perkin-Elmer Corp. (1992).
[41] H. Qin, Z. Zhang, X. Liu, Y. Zhang, J. Hu, Room-temperature ferromagnetism in CuO sol–gel powders and films, J. Magn. Magn. Mater. 322 (2010) 1994–1998, https://doi.org/10.1016/j.jmmm.2010.01.021.
[42] H. Xiao, W.A. Goddard, T. Cheng, Y. Liu, Cu metal embedded in oxidized matrix catalyst to promote CO2 activation and CO dimerization for electrochemical reduction of CO2, Proc. National Acad. Sci. 114 (2017) 6685–6688, https://doi.org/10.1073/pnas.1702405114.
[43] A. Wollbrink, K. Volgmann, J. Koch, K. Kanthasamy, C. Tegenkamp, Y. Li, H. Richter, S. Kämnitz, F. Steinbach, A. Feldhoff, J. Caro, Amorphous, turbostratic and crystalline carbon membranes with hydrogen selectivity, Carbon. N. Y. 106 (2016) 93–105, https://doi.org/10.1016/j.carbon.2016.04.062.
[44] T. Kou, S. Wang, S. Yang, Q. Ren, R. Ball, D. Rao, S. Chiovoloni, J.Q. Lu, Z. Zhang, E.B. Duoss, Y. Li, Amorphous CeO2–Cu heterostructure enhances CO2 electroreduction to multicarbon alcohols, ACS Materials Lett. (2022) 1999–2008, https://doi.org/10.1021/acsmaterialslett.2c00506.